metals

MDPI

Article

Prediction of Occurrence of Hot Cracks in Laser Cladding Heat Resistant Nickel Alloys

Rudolf Korsmik , Grigoriy Zadykyan, Stepan Tyukov * , Olga Klimova-Korsmik and Anastasiia Dmitrieva

Department of Digital Industrial Technology, Saint-Petersburg State Marine Technical University, Saint Petersburg 190121, Russia
* Correspondence: stepanbaraban1712@mail.ru

Abstract: Modern methods and technologies for the creation and processing of materials provide great opportunities for research. This work is devoted to the study of the causes of hot cracks, as well as the application of an analytical method for assessing the occurrence of hot cracks in high-temperature nickel alloys ZhS32, ZhS6U, ZhS6K, Rene 80, Rene 41, processed by laser powder cladding. In the course of the work, the process of the influence of a heat source on samples was modeled, an analysis of thermal fields and isotherms was performed, on the basis of which an analytical method was developed for finding the criterion for the pressure drop along the crystallization front in different modes and grades of alloys, to assess the tendency to form hot cracks in high-temperature nickel alloys.

Keywords: hot cracks; heat-resistant nickel alloys; differential pressure; laser powder cladding; cracking

check for updates

Citation: Korsmik, R.; Zadykyan, G.; Tyukov, S.; Klimova-Korsmik, O.; Dmitrieva, A. Prediction of Occurrence of Hot Cracks in Laser Cladding Heat Resistant Nickel Alloys. *Metals* **2023**, *13*, 1751. https://doi.org/10.3390/met13101751

Academic Editor: Amir Mostafaei

Received: 4 August 2023
Revised: 14 September 2023
Accepted: 21 September 2023
Published: 15 October 2023

Copyright: © 2023 by the authors. Licensee MDPI, Basel, Switzerland. This article is an open access article distributed under the terms and conditions of the Creative Commons Attribution (CC BY) license (https://creativecommons.org/licenses/by/4.0/).

1. Introduction

Heat resistant nickel alloys are used in a wide variety of industries where materials are exposed to high temperatures, corrosive environments and mechanical stresses. These alloys are designed to maintain strength, corrosion resistance and structural integrity at elevated temperatures, making them suitable for a variety of demanding applications. Nickel-based superalloys are widely used in nuclear reactors, steam and gas handling systems, heat exchangers, aircraft engines and other high-temperature components due to their superior high-temperature mechanical properties and microstructural stability. The metallurgical development of nickel-based heat-resistant alloys is inextricably linked to the history of the jet engine, for which the first heat-resistant alloys were developed. In order to reduce life cycle costs, as well as to provide longer service life of parts, nickel-based heat resistant alloys are used mainly because they are less susceptible to crack growth during stresses than other alloys. Therefore, the most common use of such alloys is in aviation. For example, in turbine blades, guide apparatuses, and in gas waste post-treatment systems [1,2].

Nickel has a face-centered cubic lattice at all temperatures and can be alloyed with several different elements to produce an alloy with unique properties compared to many other materials. Also, nickel exhibits extensive solid state solubility with many different metallic elements including copper, iron, chromium, molybdenum and cobalt, which act as solid solution hardeners and form the basis for many types of nickel-based alloys. As a result, heat-resistant nickel alloys are able to maintain structural integrity, strength and mechanical properties at high temperatures. In addition, the high content of chromium and molybdenum in heat-resistant nickel alloys provides good corrosion resistance [3].

The susceptibility to strain aging cracking is favored by high Ti and Al contents because they promote the precipitation of elements such as carbon, sulfur, and boron. The weldability of nickel-based alloys and susceptibility to strain-aging cracking is often

assessed qualitatively by plotting the Al content against the Ti content of the alloy. When the total level of Al and Ti for a particular alloy exceeds a critical value, it is considered difficult to weld and becomes increasingly unweldable as the Al and Ti content increases. This approximate assessment of the factors contributing to weld cracking does not take into account the microstructure changes caused by different thermomechanical treatments and heat treatment procedures [4].

Additive manufacturing and repair methods for the fabrication and repair of components that are used in high-temperature load applications are rapidly being introduced into manufacturing processes [5]. Additive manufacturing processes offer interesting opportunities to produce high-performance structures together with specially designed metallurgical characteristics. Among all additive manufacturing processes, laser powder cladding method is widely used [6,7].

Typically, the process consists of a laser source that creates a melt bath on the substrate, while the metal powder is fed from the nozzle into the melt bath and completely melted. This method has several advantages over conventional remanufacturing processes, namely low heat affected zone, minimal deformation and mixing ratio [8]. The laser cladding method allows controlling the degree of melting, resulting in a high strength bond between the powder mixture and the base layer. The process is also oxidation resistant due to the protection of the treated area by an inert gas mixture such as argon and helium.

The authors of the study [9] perform optimization of the laser cladding process by adjusting the process parameters such as laser power, scanning speed and powder feed rate to achieve high quality repairs. For this purpose, the quality and geometric characteristics of the clad single layers are evaluated by considering the contact angle between the substrate and the layer. It was found that the formation of the width of the clad layer is more influenced by the laser power at a constant scanning speed. While the scanning speed is the dominant parameter for the formation of the clad layer height, due to the effect on powder material accumulation and thermal absorption. As a result of this experiment and analysis, the most effective laser cladding mode was identified to obtain a good bonding of the clad layer with the substrate, having no cracks and low porosity content.

In the study [10], laser powder cladding method was used to repair damaged Inconel 738 alloy blades of gas pumping stations. When Inconel 625 metal powder was used, the compound has a lower hardness compared to the base metal and can be clad in the low-stress area of the blade. Whereas when cladding the blade with the same grade powder as the base metal, preheating of the part is required, also the restoration of the blade geometry is possible in more stressed areas.

Also in the study [11], the authors restored knife-edges of turbine blades in need of restoration. A nickel-based metal powder was used as an additive material, the chemical composition of which coincided with the blade material. During the process, the temperature of the melt bath was controlled by adjusting the laser power using a signal system. The cladding process resulted in restored geometry of the blade-edges, free of cracks and defects by controlling the heat input to avoid hot cracking. It was also found that all deposited layers exhibited homogeneous microhardness with Ti-dominated carbide formation at the grain boundary.

In addition, there is a gas tungsten arc method for the repair of high temperature components. For example, in a study [4], this method was used to perform the most cost-effective repair of a stator blade inlet edge made of Inconel 939 alloy, using filler wire made of the more ductile Inconel 625 alloy. This resulted in a complete joint with micro cracks that are difficult to avoid and the size of these cracks is considered acceptable.

Application and development of progressive methods of materials processing when introducing heat-resistant alloys into production are largely hampered by the destruction of the material during crystallization [12]. Nickel-based alloys crystallize in the form of austenite from the liquid phase. During crystallization due to different solubility of impurities in solid and liquid metal, segregation of alloying elements occurs and this strongly contributes to the formation of crystallization cracks in the weld. Segregation leads

to the distribution of low melting point liquid films in interdendritic spaces and along grain boundaries during the final phase of crystallization. Crystallization-induced shrinkage of the melt zone causes the accumulation of tensile strains in the weld, which can segregate the grains at the boundaries that are completely covered by the liquid [13].

Due to the fact that the technological process of laser powder surfacing is a complex science-intensive process depending on a large number of input parameters, in order to save resources, time and optimize the process as a whole, mathematical modeling methods are resorted to [14]. Although laser powder surfacing is a relatively new field, it is based on well-known welding processes [15,16]. The complexity of the laser powder surfacing process lies in the need to solve the problem of combining different physical effects occurring in the same product in volumes differing by several orders of magnitude. Modeling of the laser cladding process allows the estimation of transient stresses, residual stresses and distortions, they can be used to evaluate structural misalignments and unexpected failures due to overstress caused by the superposition of operational loads and cladding-induced residual stresses [17].

This work is devoted to the study of the causes of hot cracks, as well as the application of an analytical method for evaluating the occurrence of hot cracks in heat-resistant nickel alloys processed by laser powder cladding.

2. Methodology, Materials and Equipment

2.1. Description of the Thermal Model

Thermal processes during welding/melting as well as the thermal state determine important aspects like productivity and techno-economic efficiency. During welding/melting of metal, the temperature state varies over a wide range and is considered to be non-uniform, within this range a number of transformations take place, e.g. physico-chemical interaction with the environment, melting with crystallization of the metal, processing of the materials involved. Thermal conductivity determines the flow of a certain amount of heat per unit time through an isothermal surface, it varies with the chemical composition of the metal and temperature. In order to determine the temperature points of a body, it is necessary to determine the amount of heat that enters the body under consideration, but also to establish the heat flux the heat flux that passes through the section under consideration. The process of change of body temperature points in time for a three-dimensional body in the absence of heat exchange with the environment is described by the differential equation of heat conduction:

$$\frac{\partial T}{\partial t} = \frac{\lambda}{c\rho}\left(\frac{\partial^2 T}{\partial x^2} + \frac{\partial^2 T}{\partial y^2} + \frac{\partial^2 T}{\partial z^2}\right) = \alpha \nabla^2 T, \quad (1)$$

where $\frac{\partial T}{\partial t}$—rate of temperature change; λ—coefficient of thermal conductivity; c—specific heat capacity; ρ—density; $\frac{\partial^2 T}{\partial x^2}$, $\frac{\partial^2 T}{\partial y^2}$, $\frac{\partial^2 T}{\partial z^2}$—temperature gradient in the plane x, y, z; α—thermal diffusivity; $\nabla^2 T$—Laplace operator.

The distribution of heat from different sources can greatly complicate the final formula and calculation, so additional simplified schemes are used to classify welding heat sources.

Thus, to build a calculation model of laser powder surfacing, we assume, 2 heat sources were applied and combined, namely, a circular heat source (2) and a point heat source on the surface of a semi-infinite body (3).

$$q_2 = q_{2m} e^{(-kr2)}, \quad (2)$$

$$\Delta T = \frac{q}{2\pi\lambda R} e^{-\frac{v}{2\alpha}(R+x)}, \quad (3)$$

where q_2—heat flow power; q_{2m}—the highest heat flow in the center of the heating spot; k—heat flux concentration factor; r—radial distance from the considered point to the axis;

ΔT—temperature increment at the considered point with coordinates x, y, z; λ—coefficient of thermal conductivity; R—radius vector of a body point; v—speed; α—thermal diffusivity.

The analytical solution estimates the temperature field in a semi-infinite body when it is exposed to a moving point heat source. To solve this problem, we use PTC Mathcad Prime 4.0 software. The final calculation formula with the integration of 2 heat sources is as follows:

$$T = \iint_{-rb}^{rb} \frac{I_q(x_1, y_1)}{2\pi\lambda R(x_1, y_1)} exp(-\frac{v}{2\alpha}(R(x_1, y_1) + x - x_1))dx_1 dy_1, \quad (4)$$

at

$$I_q = \frac{q\eta}{\iint_{-rb}^{rb} exp(-\frac{x^2+y^2}{rb^2 o})dxdy} exp(-\frac{x_1^2 + y_1^2}{rb^2 o}), \quad (5)$$

$$R = \sqrt{(x - x_1)^2 + (y - y_1)^2 + z^2}, \quad (6)$$

where T—temperature increment at the considered point with coordinates x, y, z; I_q—radiation power with Gaussian distribution; λ—coefficient of thermal conductivity; R—radius vector of a body point; v—speed; α—thermal diffusivity; q—heat flow power; η—efficiency; rb—spot radius; x,y—rectangular coordinates of the fixed frame; o—source heat flux concentration coefficient; x_1,y_1—rectangular coordinates of the moving system.

2.2. Brief Description of the Formation of Dendritic Structure and Crystallization Cracks

When the molten metal cools and solidifies, the atoms begin to line up into a crystal structure. And if the cooling rate is not fast enough, the solidification front can become unstable and form irregularities. This can lead to the formation of dendrites, which sprout into the liquid metal and can cling to each other. It is also hypothesized that during solidification of a metal alloy and an abrupt change in thermal gradient, columnar dendrites are formed that grow vertically, with a single rod that branches into smaller secondary branches. Whereas with small changes in this parameter, equiaxed dendritic branches are formed. It is also worth considering that the morphology of equiaxed dendrites depends significantly on the cooling rate. As the cooling rate increases, the radius of the dendritic tips decreases until the transition from a branched dendritic system to a cellular or globular one occurs [18].

The formation of crystallization cracks is associated with a lack of supply in the solid-fluid zone, but only for certain regions where the dendritic skeleton is subjected to shear or tensile stresses. When the dendritic network is coherent, it can withstand and actually transmit stresses as well. Above the coherence temperature, the fluid still present between the dendrites is continuous because the solidified branches of the dendrites have not yet joined. Consequently, deformation induced by thermal stresses can disconnect these branches quite easily. In the case of the ability of interdendritic fluid flow to feed such regions, the existence of localized reverse segregation of hot crack healing is possible. However, deep in the solid-liquid zone, where its permeability is very low, the opening of the incoherent dendritic skeleton under the action of tensile strain cannot be compensated by the liquid [19].

2.3. Description of the Cracking Criterion

The authors of the study [20] introduced a new criterion for detecting hot cracks in metal alloys, which is based on balancing the masses of liquid and solid phases. Figure 1 shows the second-order growth pattern of columnar dendrites, which illustrates the formation of hot cracks in a metal. As noted earlier, it is assumed that the dendritic network grows at a certain thermal gradient (G) and at a certain velocity of the liquidus isotherm (v_l). This velocity is directed opposite to the direction of dendrite growth in order to compensate for shrinkage, since the specific mass of the solid is greater than the mass of the liquid for most metal alloys. The dendritic network may be subjected to tensile strain that is

perpendicular to dendrite growth, thus the fluid flow must compensate for this strain if hot cracks are not to form.

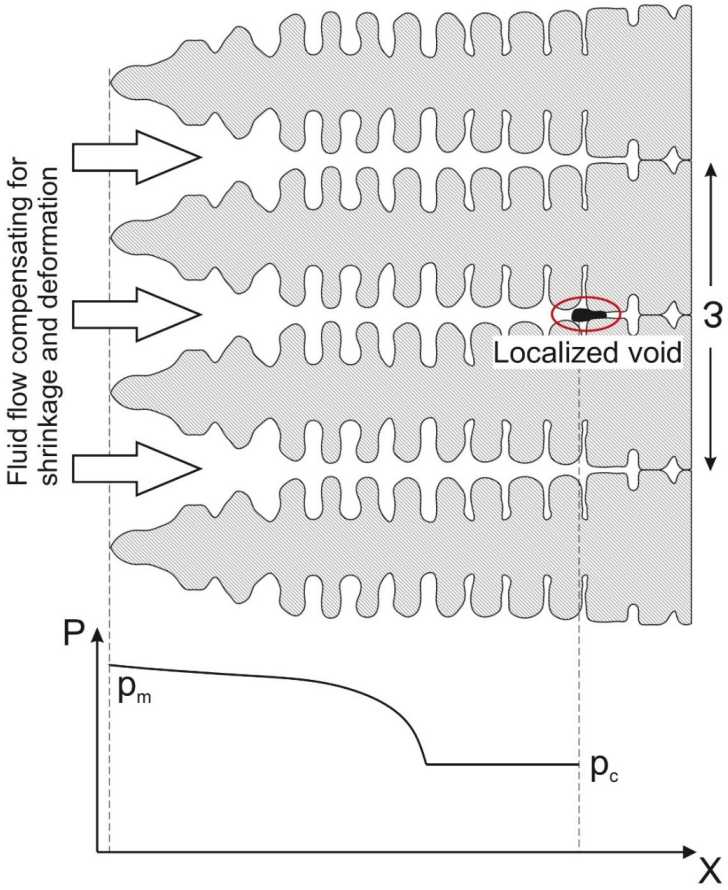


Figure 1. Schematic of second-order growth of columnar dendrites.

The figure also shows a graph of pressure change in the interdendritic fluid, where it can be seen that the metallostatic pressure (p_m), located at the tip of the dendrites, decreases as it approaches the base of the dendritic branches. If the pressure falls below the cavitation pressure (p_c), there is a high chance of voiding, indicated in black in the figure, resulting in the formation of hot cracks.

To evaluate the nucleation of hot cracks in heat-resistant nickel alloys, we use the method used in the study [20] under deformation conditions when the pressure in the interdendritic fluid is reduced to a critical value. The formula for finding the critical pressure (p_{max}) at which a hot crack is formed is presented next:

$$p_{max} = \Delta p_\epsilon + \Delta p_{sh} = \Delta p_c = p_m - p_c, \tag{7}$$

where p_{max}—differential pressure until reaching a critical value—cavitation pressure; Δp_ϵ—pressure drop associated with deformation; p_{sh}—shrinkage pressure drop; Δp_c—cavitation pressure; p_m—metallostatic pressure.

Over the entire length of the solid-liquid region, the maximum pressure drop between the roots and tops of the dendrites is expressed by the equation:

$$p_{max} = (1+\beta)\mu \int_{T_c}^{T_l} \frac{E}{K} dx + \upsilon\beta\mu \int_{T_c}^{T_l} \frac{f_l}{K} dx, \tag{8}$$

at

$$E(x) = \int f_s \dot{\epsilon_p} dx, \tag{9}$$

where β—shrinkage factor; μ—dynamic viscosity; T_l—liquidus temperature; T_c—coherence temperature; E—accumulated strain rate; K—fluid permeability of the dendritic skeleton; v—crystallization front speed; f_l—amount of liquid phase; f_s—amount of solid phase; $\dot{\epsilon_p}$—strain rate.

Expressing the permeability K by the Karman-Kozeny equation:

$$K = \frac{\lambda_2^2}{180} \frac{(1-f_s)^3}{f_s^2}, \tag{10}$$

and replacing the x-coordinate with the temperature, we get:

$$\Delta p_{max} = \frac{180(1+\beta)\mu}{\lambda_2^2 G} \int_{T_c}^{T_l} \frac{E(T) f_s(T)^2}{(1-f_s(T))^2} dT + \frac{180\beta\mu v}{\lambda_2^2 G} \int_{T_c}^{T_l} \frac{f_s(T)^2}{(1-f_s(T))^2} dT, \tag{11}$$

at

$$E(T) = \frac{1}{G} \int f_s(T) \epsilon_p(T) dT, \tag{12}$$

where λ_2—distance between axes of second-order dendrites; G—temperature gradient.

2.4. Materials Used

Powder materials of heat-resistant nickel alloys ZhS32, ZhS6K, ZhS6U, Rene 41 and Rene 80 were used for conducting laser powder cladding experiments. The chemical composition of the alloys is shown in Table 1. The fraction of powder materials was 45–120 microns, the shape of the powders is spherical.

Table 1. Chemical composition of heat-resistant alloys.

Alloy Grade	Content of Elements, % (by Mass)										
	Ni	Cr	Al	Co	Ti	Nb	Mo	W	C	Ta, Re	Fe
ZhS32	basis	7.7	5.2	7.2	-	1.6	1.0	8.7	0.15	3.5–4.5	<1.0
ZhS6K	basis	11.3	5.5	4.5	2.8	-	4.0	5.0	0.16	-	<2.0
ZhS6U	basis	8.8	5.6	9.8	2.4	1.0	1.8	10.3	0.17	-	<1.0
Rene 80	basis	13.9	3.5	9.6	4.9	-	4.0	3.9	0.17	-	<1.0
Rene 41	basis	19	1.6	11	3.2	-	9.5	-	0.09	-	<5.0

2.5. Laser Powder Cladding Equipment and Experiment Setup

Experimental studies were carried out on the robotic complex for laser powder surfacing ILIST-M (Figure 2a), which includes an IPG YLR-1500-U ytterbium fiber laser, cooling system of the SMC HRSH090-A-40 unit, 6-axis Fanuc M-10iD/12 robot manipulator, IPG FLW D30L process head (Figure 2b), product handling system based on a single-axis positioner (Figure 2c). The optical system of the laser head includes a collimator with a focal length of 100 mm. To transport laser radiation from the source to the head, a transport fiber with a diameter of 100 µm is used.

The process tool is positioned perpendicular to the substrate at a distance of 150 mm from the nozzle shear to the metal substrate, while maintaining this distance throughout the process. The substrates were grades of heat-resistant nickel alloys used for manufacturing gas turbine engine blades. The laser beam spot forms a melt bath on the substrate surface and at the same time a compressed gas powder jet is fed coaxially to the laser beam using a jet nozzle (Figure 2d), with argon used as the transport gas. The metal powder crystallises in the melt bath, thereby forming a roll or layer. As a result, walls with a length of 50 mm and a height of 9–11 mm were obtained. The number of clad layers is 100–120.

The methodology of experiments on laser powder cladding of heat-resistant nickel alloys consisted of cladding of single walls in edge modes. These modes were selected based on the available experience with heat-resistant alloys.

Technological parameters of the laser cladding process are presented in Table 2.

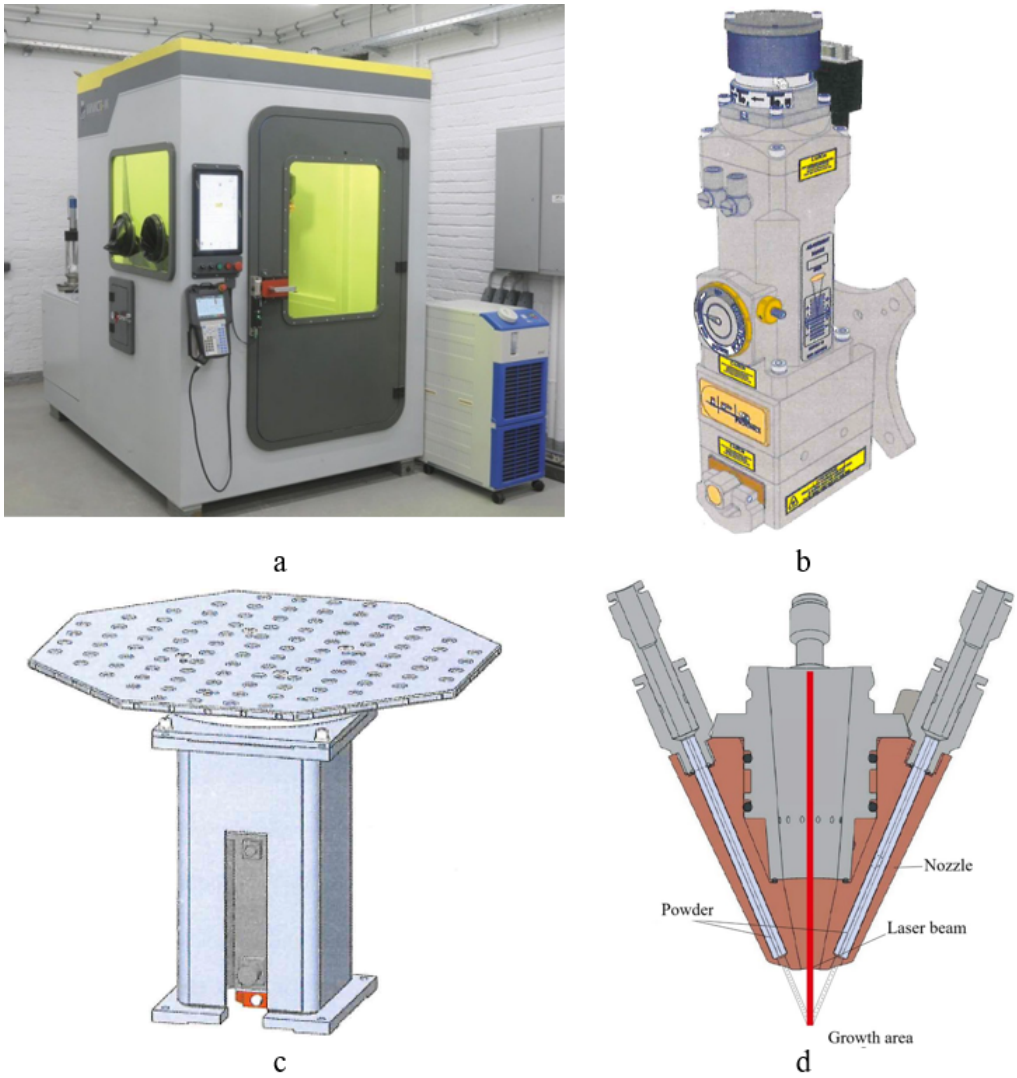


Figure 2. (**a**) technological complex ILIST-M; (**b**) laser optical head; (**c**) single-axis positioner; (**d**) powder feeding nozzle.

Table 2. Modes of laser cladding.

Alloy Grade	№	Power, W	Speed, mm/s	Powder Consumption, g/min
ZhS32	1 2	200 1000	3 15	2.4 11.6
ZhS6K	3 4	200 1000	3 15	2.4 11.6
ZhS6U	5 6	200 1000	3 15	2.4 11.6
Rene 41	7 8	200 1000	3 15	2.4 11.6
Rene 80	9 10	200 1000	3 15	2.4 11.6

2.6. Study of the Macrostructure of Samples

The clad specimens were visually inspected (Figure 3) for the presence/absence of obvious defects (cracks, unstable areas, etc.).

At the end of visual inspection, the clad samples were prepared for further metallographic examination. The samples obtained as part of the experimental studies were

examined using a Leica DMi8A inverted metallographic microscope and a TESCAN MIRA 3 scanning electron microscope.

Macro-slides of clad layers of ZhS32 and Rene 80 with and without cracks are presented in Figure 4.



Figure 3. Appearance of the clad walls. 1—ZhS32 in laser cladding mode №1, 2—ZhS32 in laser cladding mode №2.



Figure 4. Longitudinal and transverse sections of alloys: (**a**) ZhS32, (**b**) Rene 80.

According to the results of visual inspection of the obtained specimens, they can be classified as: clad specimens with stable formation with no cracks/non-melting and clad specimens with unstable formation with cracks/non-melting.

Figure 3 shows a number of defects, including cracks formed in large numbers. Further, when analyzing the macrostructure of cross-sectional and longitudinal sections of the clad walls, in a number of samples there were found cracks, passing mainly along the grain boundaries of the clad metal, as well as the accumulation of pores of various sizes.

3. Research Results

3.1. Results of Thermal Calculations

By analytically solving thermal problems based on Formulas (4)–(6), we obtain the temperature distribution and, for further analysis, construct isotherms in several planes. Further in Figure 5, the temperature distributions along the *x*-axis and along the *y*-axis, respectively, for the ZhS32 sample are presented. The plots were obtained in PTC Mathcad Prime 4.0 software.

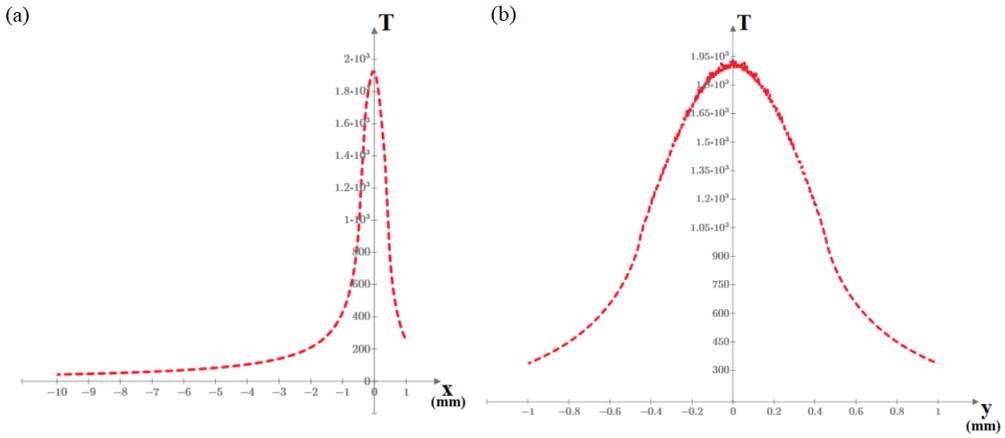


Figure 5. Temperature distribution along the axes: (**a**) x, (**b**) y.

It can be seen from the graphs that the maximum temperature reaches 1943 °C, since there are errors near the impact of a heat source, the cross-section graph is displayed incorrectly in the region of the extremum point, it should also be taken into account that these graphs were obtained at a depth of fractions of a millimeter, and not on the surface sample to avoid error. Further, Figure 6, show the isotherms in three planes, obtained as a result of calculations for the sample ZhS32, the units of measurement of the axes of the graphs are also presented in millimetres.

From the isotherm in the top view, it can be seen that the weld pool practically takes the form of a spherical shape, which may well occur in laser powder cladding. Having calculated the distance between the liquidus and solidus temperature isotherms, we determine the temperature gradient to determine the pressure drop. The results of the obtained calculations of the temperature gradient are presented in Table 3.

Table 3. Results of temperature gradient calculations.

Alloy Grade	Technological Mode	
	200 W, 3 mm/s	**1000 W, 5 mm/s**
ZhS32	2.3×10^6 K/m	9.3×10^5 K/m
ZhS6K	2.4×10^6 K/m	8.9×10^5 K/m
ZhS6U	1.9×10^6 K/m	8.4×10^5 K/m
Rene 80	2.9×10^6 K/m	9.5×10^5 K/m
Rene 41	5.2×10^6 K/m	8.6×10^5 K/m

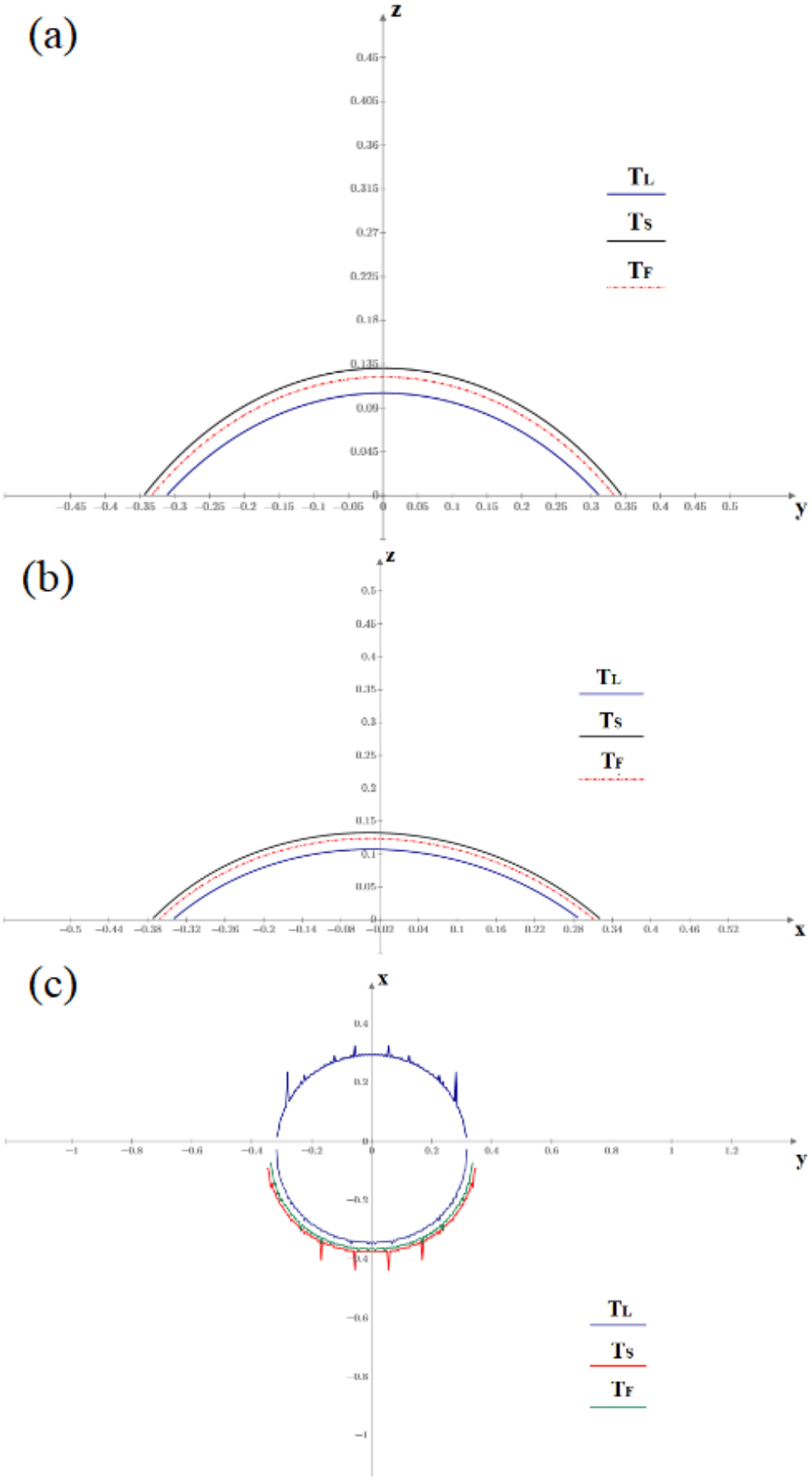


Figure 6. Isotherms: (**a**) cross section, (**b**) longitudinal section, (**c**) top view.

3.2. The Results of the Calculation of the Criterion for the Occurrence of Cracks

Analytical calculations were made according to Formula (11). As a result of calculations, we obtain a number of values presented in Table 4.

Table 4. Results of pressure drop calculation

Alloy Grade	Technological Mode	
	200 W, 3 mm/s	1000 W, 5 mm/s
ZhS32	7.91 MPa	165.49 MPa
ZhS6K	10.13 MPa	217.44 MPa
ZhS6U	6.42 MPa	195.74 MPa
Rene 80	14.45 MPa	318.82 MPa
Rene 41	10.11 MPa	263.71 MPa

Further, the resulting thermophysical characteristics of the crystallization of alloys are translated into technological processing parameters and we obtain a graph of three-dimensional graphs, which are presented in Figures 7 and 8, the dependence of the pressure drop on such parameters as power and speed, as well as on speed and temperature gradient, respectively.

From the obtained graphs we can conclude that the pressure drop along the crystallisation front (p_{max}) increases with the increase of such parameters as power, laser head rotation speed, because the residual liquid (melt) forms a continuous thin layer between the branches of dendrites, thus preventing them from touching. At the same time, the highest value of the pressure drop is observed in the Rene 41 alloy, among other alloys, both in the mode of 200 W, 3 mm/s, and in the mode of 1000 W, 15 mm/s. On the basis of the obtained results of calculating the criterion for the occurrence of hot cracks, it is possible to distinguish alloys from less prone to cracking to the most prone: ZhS32, ZhS6U, ZhS6K, Rene 80, Rene 41.

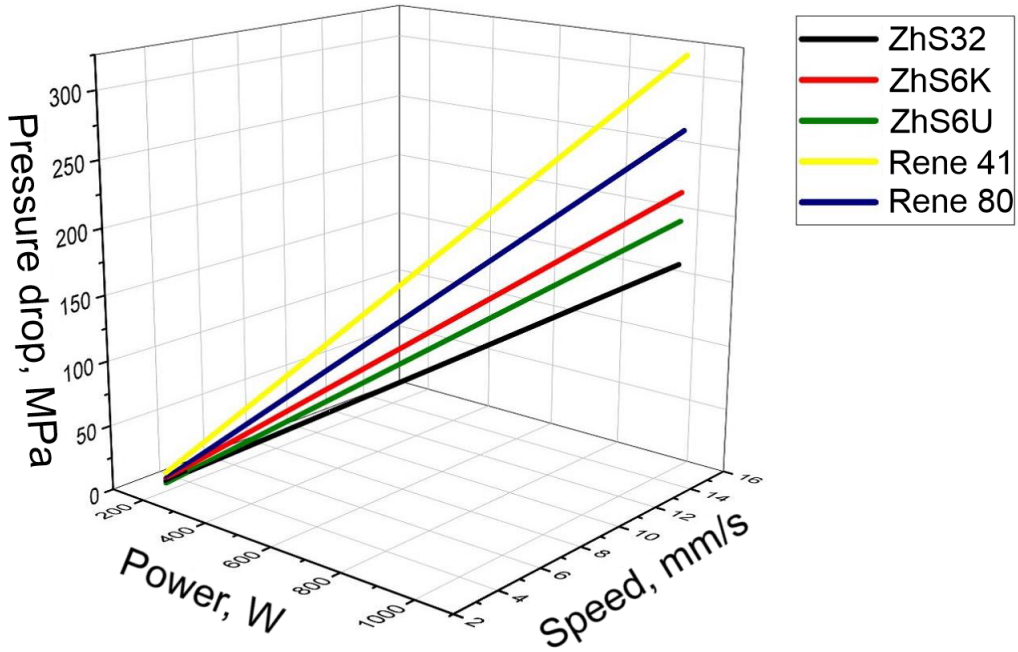


Figure 7. Graph of the dependence of pressure drop on power and speed.

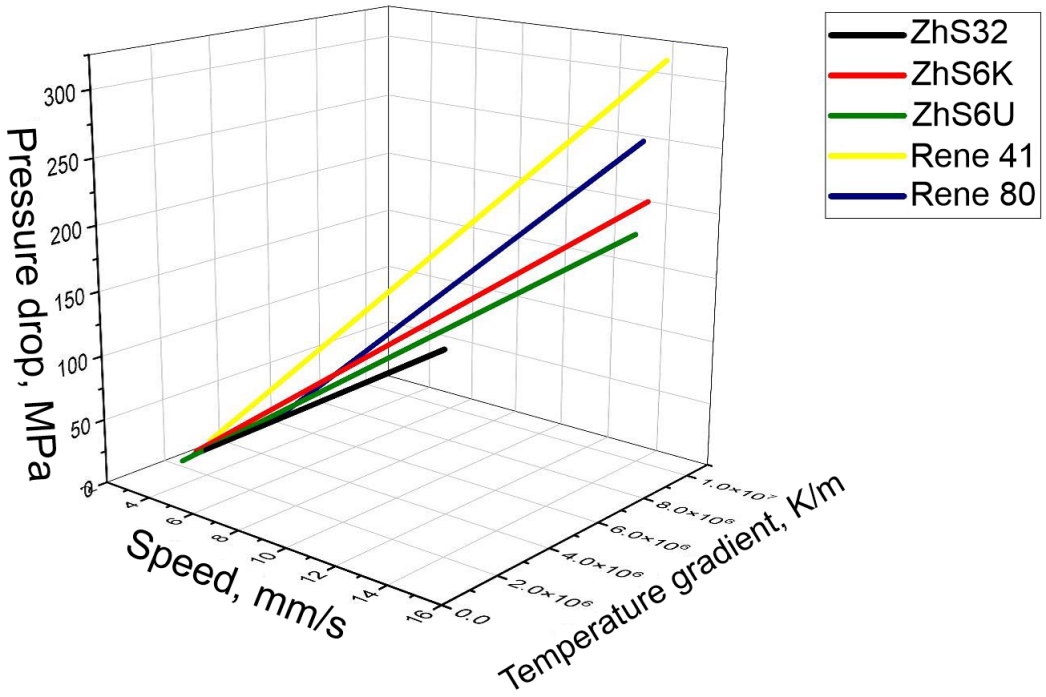


Figure 8. Plot of pressure drop versus velocity and temperature gradient.

4. Conclusions

In the course of the work, the process of the influence of a heat source on samples was modeled, an analysis of thermal fields and isotherms was performed, on the basis of which an analytical method was developed for finding the criterion for the pressure drop along the crystallization front in different modes and grades of alloys, to assess the tendency to form hot cracks in high-temperature nickel alloys.

Based on the data obtained, it can be said that the pressure drop along the crystallization front, performed in the mode of 200 W, 3 mm/s for all alloy grades, varies in a small range of values from 6.43 to 14.45 MPa, it is also worth noting that under this mode, hot cracks were not observed on the sections of heat-resistant alloys. The most susceptible alloy to hot cracks in this mode is Rene 41, while ZhS6U is the least susceptible to hot cracks.

Based on the results of surfacing in the 1000 W, 15 mm/s mode, it can be said that the obtained values of the pressure drop along the solidification front vary from 165.49 to 318.82 MPa, which differs significantly from the previous mode. Cracks are present in all deposited specimens. The alloy most susceptible to hot cracking in this mode is Rene 41, while ZhS32 is the least susceptible to hot cracking.

Author Contributions: Conceptualization, A.D. and G.Z.; methodology, G.Z.; software, S.T.; validation, R.K., G.Z. and O.K.-K.; formal analysis, G.Z. and S.T.; investigation, A.D., G.Z. and S.T.; resources, R.K.; data curation, G.Z. and S.T.; writing—original draft preparation, G.Z. and S.T.; writing—review and editing, S.T.; visualization, S.T.; supervision, O.K.-K.; project administration, O.K.-K. and R.K.; funding acquisition, O.K.-K. All authors have read and agreed to the published version of the manuscript.

Funding: This research was funded by the Ministry of Science and Higher Education of the Russian Federation as part of World-class Research Center program: Advanced Digital Technologies [contract No. 075-15-2022-312 dated 20 April 2022]; and the Russian Foundation for Basic Research (RFBR) within the framework of the Theoretical and Experimental Investigations of the Metallurgy of Nickel Phase Transformations [project number 21-58-12019] "Studies of the Metallurgy of Phase Transformations in Nickel Superalloys for conditions of multiple thermocycling at DMD based additive process".

Data Availability Statement: Data sharing is not applicable.

Conflicts of Interest: The authors declare no conflict of interest. The funders had no role in the design of the study; in the collection, analyses, or interpretation of data; in the writing of the manuscript, or in the decision to publish the results.

References

1. Amato, K.N.; Gaytan, S.M.; Murr, L.E.; Martinez, E.; Shindo, P.W.; Hernandez, J.; Collins, S.; Medina, F. Microstructures and mechanical behavior of Inconel 718 fabricated by selective laser melting. *Acta Mater.* **2012**, *60*, 2229–2239. [CrossRef]
2. Dinda, G.P.; Dasgupta, A.K.; Mazumder, J. Texture control during laser deposition of nickel-based superalloy. *Scr. Mater.* **2012**, *67*, 503–506. [CrossRef]
3. Caron, J.L.; Sowards, J.W. Weldability of nickel-base alloys. In *Comprehensive Materials Processing*; Elsevier: Amsterdam, The Netherlands, 2014; pp. 151–179.
4. Henderson, M.B.; Arrell, D.; Larsson, R.; Heobel, M.; Marchant, G. Nickel based superalloy welding practices for industrial gas turbine applications. *Sci. Technol. Weld. Join.* **2013**, *9*, 13–21. [CrossRef]
5. Korsmik, R.S.; Turichin, G.A.; Zadykyan, G.G.; Zhitenev, A.I. Investigation of Crystallization Process of a Single Crystal Nickel-Based Alloy during the Laser Multilayer Cladding. *Key Eng. Mater.* **2019**, *822*, 481–488. [CrossRef]
6. Weisheit, A.; Gasser, A.; Backes, T.; Jambor, N.; Pirch, K.; Wissenbach, K. *Direct Laser Cladding, Current Status and Future Scope of Application*; Springer: Berlin/Heidelberg, Germany, 2013; pp. 221–240._5. [CrossRef]
7. Gu, G. Laser additive manufacturing (AM): Classification, processing philosophy, and metallurgical mechanisms. In *Laser Additive Manufacturing of High-Performance Materials*; Springer: Berlin/Heidelberg, Germany, 2015; pp. 15–71._2. [CrossRef]
8. Turichin, G.A.; Klimova-Korsmik, O.G.; Valdaytseva, E.A.; Alekseev, A.V.; Rashkovets, M.V. Comparative analysis of the gamma prime phase formation in nickel alloys in additive manufacturing. *Procedia CIRP* **2020**, *94*, 320–323. [CrossRef]
9. Zhu, S.; Chen, W.; Zhan, X.; Ding, L.; Zhou, J. Parameter optimisation of laser cladding repair for an Invar alloy mould. *Proc. Inst. Mech. Eng. Part B J. Eng. Manuf.* **2019**, *233*, 1859–1871. [CrossRef]
10. Chen, C.; Wu, H.C.; Chiang, M.F. Laser cladding in repair of IN738 turbine blades. *Int. Heat Treat. Surf. Eng.* **2008**, *2*, 140–146. [CrossRef]
11. Guijun, B.; Andres, G. Restoration of Nickel-Base Turbine Blade Knife-Edges with Controlled Laser Aided Additive Manufacturing. *Phys. Procedia* **2011**, *12*, 402–409.
12. Shorshorov, M.H.; Erokhin, A.A.; Chernyshova, T.A.; Kotov, G.N.; Russian, A.V. Hot cracks in welding of heat-resistant alloys. *Mashinostroenie* **1973**, *224*, 115–119.
13. Korsmik, R.S. Laser Powder Cladding of the Heat-Resistant Nickel Alloy ZHs 32 on the Working Blades of Gas-Turbine Engines. Ph.D. Thesis, Candidate of Technical Sciences, State Marine Technical University, Saint-Petersburg, Russia, 2021.
14. Peralta, A.D.; Enright, M.; Megahed, M.; Gong, J.; Roybal, M.; Craig, J. Towards rapid qualification of powder bed laser additively manufactured parts. *Integr. Mater. Manuf. Innov.* **2016**, *5*, 154–176. [CrossRef]
15. Tejc, J.; Kovařík, J.; Zedník, V.; Sholapurwalla, A.; Nannapuraju, M.; Porzner, M.; Boitout, F. Using numerical simulation to predict the distortion of large multi-pass welded assemblies. In Proceedings of the 12th International Conference on Modeling of Casting, Welding, and Advanced Solidification Processes, Vancouver, BC, Canada, 7–14 June 2009; Volume 8.
16. Bergheau, J.M.; Robin, V.; Boitout, F. Finite element simulation of processes involving moving heat sources—Application to welding and surface treatment. In Proceedings of the 1st International Conference on Thermal Process Modelling and Computer Simulation, Shanghai, China, 20–22 November 2000; Volume 9.
17. Tsirkas, S.A.; Papnikos, P.; Kermanidis, T. Numerical simulation of the laser welding process in butt-joint specimens. *J. Mater. Process. Technol.* **2003**, *134*, 59–69. [CrossRef]
18. Stefanescu, D.; Ruxanda, R. *Fundamentals of Solidification*; The University of Alabama: Tuscaloosa, AL, USA, 2004; pp. 71–92.
19. Campbell, J. *Castings*, 2nd ed.; Elsevier: Burlington, NJ, USA, 2003; p. 352.
20. Rappaz, M.; Drezet, J.-M.; Gremaud, M. A New Hot-Tearing Criterion. *Metall. Mater. Trans. A* **1999**, *30*, 449–455. [CrossRef]

Disclaimer/Publisher's Note: The statements, opinions and data contained in all publications are solely those of the individual author(s) and contributor(s) and not of MDPI and/or the editor(s). MDPI and/or the editor(s) disclaim responsibility for any injury to people or property resulting from any ideas, methods, instructions or products referred to in the content.